Effect of Dy^{3+} substitution on microwave behaviour of nanocrystalline Mn-Zn Ferrite

P. Neelima[1] and S. R. Murthy[1, 2]*

[1]*Department of Physics, Osmania University, Hyderabad 500 007, India.*
[2]*Geethanjali college of Engineering and Technology, Cheeryal, Hyderabad 501301*

*Corresponding author

DOI: 10.5185/amp.2018/6681
www.vbripress.com/amp

Abstract

Microwave-hydrothermal (M-H) method had been employed to synthesize a series of Dy^{3+}doped Mn-Zn ferrite $Mn_{0.6}Zn_{0.4}Fe_{2-x}Dy_xO_4$ (x=0, 0.01, 0.03, 0.05, 0.07, 0.09) nanopowders at 160°C/30 min. The prepared samples have been characterized by Fourier Transform Infrared Spectrometer. The grain size of sintered ferrites are in the range of 60-70 nm. Decrease in saturation magnetization and increase in coercivity were observed with an increase of Dy^{3+} concentration in Mn-Zn ferrites. The complex permeability and complex permittivity of the prepared samples were measured in the frequency range of 2–18 GHz using a using a vector network analyzer. It is observed that small variation of Dy^{3+} substitution in spinel ferrite tailored microwave absorbing parameters dramatically. The reflection loss (RL) increased with the Dy^{3+} content upto $x \leq 0.03$. The sample with x=0.03 of thickness 2.3 mm showed minimum reflection loss of -20.5 dB with a bandwidth of 3.8 GHz. Thus the present materials exhibit good microwave absorption properties and hence can act as EMI suppressors.

Keywords: Spinel ferrite, microwave hydrothermal method, doping, complex permittivity, complex permeability, microwave absorption properties.

Introduction

Due to the rapid development of microwave technology in recent years in the fields of wireless telecommunication systems, military, medical applications etc., the problem of electromagnetic interference (EMI) pollution is a major concern. There is a great demand in developing different types of new materials in order to suppress the EMI in high frequency of GHz range **[1]**. During last decade, several EMI shielding materials have been developed such as spinal ferrites**[2,3]**, hexaferrites**[4,5]**, spinel ferrite/polymer composites**[6,7]**, hexaferrite/polymer composites**[8,9]**, carbon nanotubes composite**[10,11]** etc. However, exploring the development of novel materials possessing enhanced microwave absorbing properties such as reflection loss with broad band width, shielding effectiveness, etc. in GHz frequency range is a challenging task.

Spinel ferrites are considered as good microwave absorbing materials due to their excellent dielectric and magnetic properties like high complex permeability, high magnetic saturation, low magnetic loss and high resistivity **[12, 13]**. To enhance the properties required for microwave absorbers, studies on spinal ferrites with rare earth doped ions have been investigated **[14,15]** and showed that doping is an effective approach since rare earth doped ions establish strong 4f-3d spin orbit coupling which improve electrical and magnetic properties.

Mn-Zn ferrite possess better electrical and magnetic properties among other spinel ferrites**[16]**.There are no systematic studies being reported so far on doped Mn-Zn ferrites for EMI suppressor applications. Since Dy^{3+} has large ionic radius, it possess typical relaxation characteristics which influence the electromagnetic properties of ferrite when doped **[17]**. Thus in our present work, we have selected and synthesized Mn-Zn spinel ferrite doped with small amounts of Dy^{3+} ion, by microwave hydrothermal method and studied electromagnetic properties in the frequency range 2-18 GHz.

Experimental

Nanopowders with the composition $Mn_{0.6}Zn_{0.4}Fe_{2-x}Dy_xO_4$ (x=0, 0.01, 0.03, 0.05, 0.07, 0.09) were synthesized using microwave-hydrothermal (M-H) method. Manganese nitrate [$Mn(NO_3)_2.\ 6H_2O$] (purity 99.99%), Zinc nitrate[$Zn(NO_3)_2\ .6H_2O$] (purity 99.99%), Dysprosium nitrate [$Dy\ (NO_3)_3.6H_2O$] (purity 99.98%) and Iron nitrate [$Fe(NO_3)_3.9H2O$] (purity 99.98%) all from Sigma Aldrich are used as starting chemicals. The metal salts were dissolved in 40 ml of de-ionized water followed by addition of NaOH solution with constant stirring and at controlled pH. The precipitate was obtained at pH~ 9.5.The solution was then transferred into a tetrafluorometoxil (TFM) reaction vessel. The TFM vessel was then mounted on the turntable in the microwave equipment (model MARS-5, CEM corp. Mathews, NC) for microwave treatment (frequency 2.45 GHz). The sample solution in the microwave was exposed to 160^0C with holding time of 30min at 300 W. Later the product was centrifuged, washed repeatedly

with water and then filtered. The precipitate was dried overnight at 65°C.

As synthesized powder was characterized using Fourier transform Infrared [FTIR, Brucker tensor 27] spectroscopy at room temperature.

The nanopowders were uniaxially pressed into toroidal samples and pellets. The samples were sintered at 900°C/30 min using microwave sintering method. The sintered samples were characterized by X-ray diffraction (XRD) spectrum using X-Pert PAN Analytical diffractometer with CuKα radiation (wavelength λ = 1.5406 Å) and morphological studies on samples were undertaken using Scanning Electron Microscope (SEM).[SEM; Model JEOL, Tokyo, Japan]

The magnetic properties such as saturation magnetization (M_S) and coercive field (H_C) were obtained from hysteresis curves that were recorded using Vibrating Sample Magnetometer (VSM, Model DMS 1660VSM) at room temperature. The complex scattering parameters that correspond to the reflection (S11 or S22) and transmission (S21 or S12) in the samples were measured in the frequency range of 2–18 GHz using a vector network analyzer (Agilent 8722ES). The parameters ε', ε", μ' and μ" were then determined from the measured scattering parameters using Agilent software module 85071. The frequency dependence of RL at a thickness of 2.3 mm for single layer absorber was calculated.

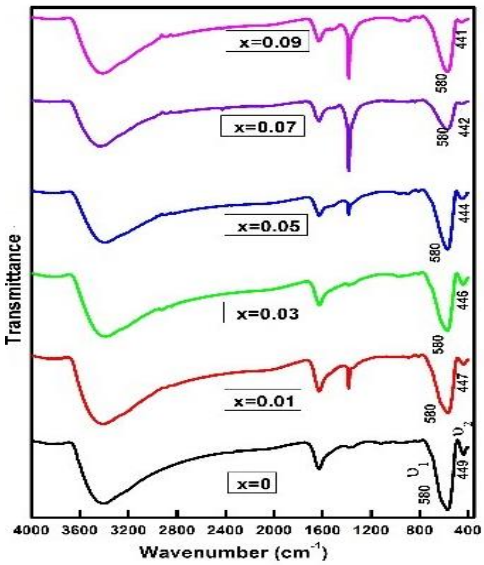

Fig. 1. FTIR spectra for as synthesized $Mn_{0.6}Zn_{0.4}Fe_{2-x}Dy_xO_4$ ($0 \leq x \leq 0.09$) nanopowders.

Results and discussion

FTIR spectra of $Mn_{0.6}Zn_{0.4}Fe_{2-x}Dy_xO_4$ ($0 \leq x \leq 0.09$) as synthesized nanopowders is shown in **Fig. 1**. Major bands of spinel ferrite, corresponding to higher frequency band (ν_1) 600–550cm^{-1}) and lower frequency band (ν_2) (450–400cm^{-1}) in IR spectra attribute to intrinsic stretching vibrations of the metal ions at tetrahedral A-site and octahedral-metal complexes respectively **[18]**. From the figure, the higher frequency band (ν_1) is seen at 580 cm^{-1} for all samples but lower frequency band ranged from 449-441 cm^{-1}. It can be observed from the figure that there is no shift in higher frequency band (ν_1) while lower frequency band (ν_2) slightly shifts to the low frequency region, with increase in substitution. This may be due to substitution of Fe3+ ions with Dy^{3+} ion at octahedral B sites. This shift in band is co-related to the variation in the cation-oxygen bond lengths at octahedral lattice of the spinel. The replacement of Fe^{3+}ions by larger Dy^{3+}ions will lead to increase in metal-oxygen bond length and consequently decrease the wave number of ν_2 band. The bands corresponding to 3400 cm^{-1}and 1600 cm^{-1}represent stretching and bending vibrations of H–O–H . The band at 1379 cm^{-1} is ascribed to the anti-symmetric stretching vibration of nitrate group.

The XRD patterns of sintered $Mn_{0.6}Zn_{0.4}Fe_{2-x}Dy_xO_4$ for $0 \leq x \leq 0.09$ samples are shown in **Fig. 2.** It is observed that the XRD patterns show good crystallization with characteristic peaks of (2 2 0), (3 1 1), (4 0 0), (4 2 2), (5 1 1), (4 4 0) and (533) which are well tallied with the reported values of JCPDS card no.74-2401. Single phase cubic spinel Mn-Zn ferrite is observed for substituted amount $x \leq 0.03$, confirming Dy^{3+} ions has completely dissolved in spinel lattice. But for samples x>0.03, there exists a small additional peak corresponding to $DyFeO_3$ phase. Due to Low solubility of Rare earth elements, doped ferrites exhibit additional crystalline peaks **[19]**. The reasons may be (i) uneven distribution of cations among tetrahedral(A) and octahedral(B) sites leading to phase inhomogeneity **[20]** (ii) larger ionic radii of Dy^{3+}ions(0.92Å) than Fe^{3+}ions(0.64Å), which limits its substitution and forms a phase on the grain boundaries **[21]**. Scherer's equation has been employed to calculate Crystallite size. The average crystallite size of sintered samples varies between 35 to 45 nm.

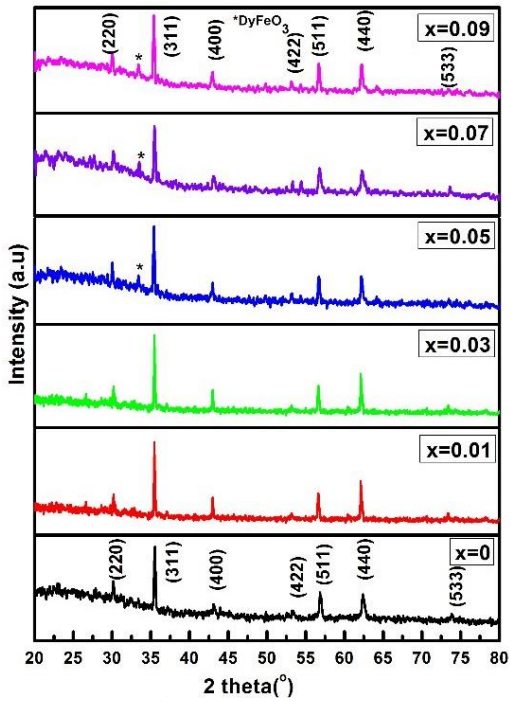

Fig. 2. XRD patterns for sintered $Mn_{0.6}Zn_{0.4}Fe_{2-x}Dy_xO_4$ ($0 \leq x \leq 0.09$) samples.

Table 1: Properties of $Mn_{0.6}Zn_{0.4}Dy_xFe_{(2-x)}O_4$ nanocrystalline ferrites measured at room temperature.

Sample name (x)	Crystallite size (nm)	Lattice constant (Å) ±0.001	Bulk Density (gm/cm^3) ±0.001	X-ray density (gm/cm^3) ±0.001	Grain size (nm)	Magnetisation M_s(emu/gm)	Coercivity H_c (Oe)	Minimum RL (-dB)
0	35	8.385	4.918	5.289	61	45	16	18.31
0.01	37	8.387	4.964	5.338	62	43	18	18.49
0.03	39	8.390	5.031	5.353	63	41	20	20.5
0.05	42	8.395	4.984	5.360	66	40	21	16.31
0.07	43	8.398	5.064	5.446	68	37	22	15.34
0.09	45	8.410	5.123	5.450	70	36	23	-

Using XRD patterns, the lattice constant has been calculated and it is observed from the **Table 1** that the values increased with increase in dopant concentration. Such enhancement in lattice constant is due to the difference in ionic radii of Dy^{3+} and Fe^{3+} ions. The Dy^{3+} ions are accommodated on the lattice, results in lattice strain. This distortion is related to changes in the Dy^{3+}–O– Fe^{3+}bond lengths.

The X-ray density of the samples is calculated as per equation 1

$$\rho_x = \frac{8M}{Na^3} \quad (1)$$

where, M is the molecular weight of the sample, N is the Avogadro's number and a^3 the volume of the cubic unit cell. X-ray density (ρ_x) varied with dopant concentration. Similar to the lattice constant, X-ray density (ρ_x) also increased with the increase in Dy^{3+} substitution. The X-ray density increases from 5.289 to 5.450 g/cc.

The bulk density for all the samples has been measured using Archimedes principle and given in the **Table 1**. The porosity of samples varies from 6-8% with doping concentration. It is observed that porosity minimized after secondary phase formation due to dopant Dy^{3+} in Mn-Zn spinel ferrite. The secondary phase restrains the grain growth and excludes the intergranular porosity [22]. Crystallite size, bulk density and lattice constant have been tabulated in **Table 1**.

The morphology of ferrite samples is studied using SEM micrographs (**Fig. 3)**. It is noted that agglomeration resulted as the nanocrystals aggregated to get low surface energy state. It is observed from **Table 1** that grain size increased with increase in Dysprosium concentration. Like crystallite size, the grain size from the SEM micrograph is also found to be larger indicating every grain is formed by aggregation of a large number of crystallites or particles.

The room temperature magnetization measurements (M-H curves) were recorded by vibrating sample magnetometer (VSM). The hysteresis (M-H) loops obtained for all the samples are shown in **Fig. 4** which depicts the nature of soft magnetic material. Saturation magnetization obtained from graph decreased with increase in Dy^{3+}concentration (Table1). The observed trend is due to the 4f electrons and their magnetic dipolar orientation of Dy^{3+} ions, are in disorder state at room temperature **[23]**.

Magnetic moment decreases due to weaker nature of Dy^{3+}-Fe^{3+} and Dy^{3+}-Dy^{3+} interaction compared to Fe^{3+}-Fe^{3+}super exchange interactions which govern magnetic nature of Mn-Zn ferrite. Reduced magnetic moment is observed in Dy^{3+}doped samples although Dy^{3+} magnetic moment(10.5μ_B) is larger than that of Fe^{3+}(5 μ_B**) [24,25]**. $DyFeO_3$ have a distorted perovskite structure in which the. Fe^{3+} spins form an antiferromagnetic order along the axis **[26]**.

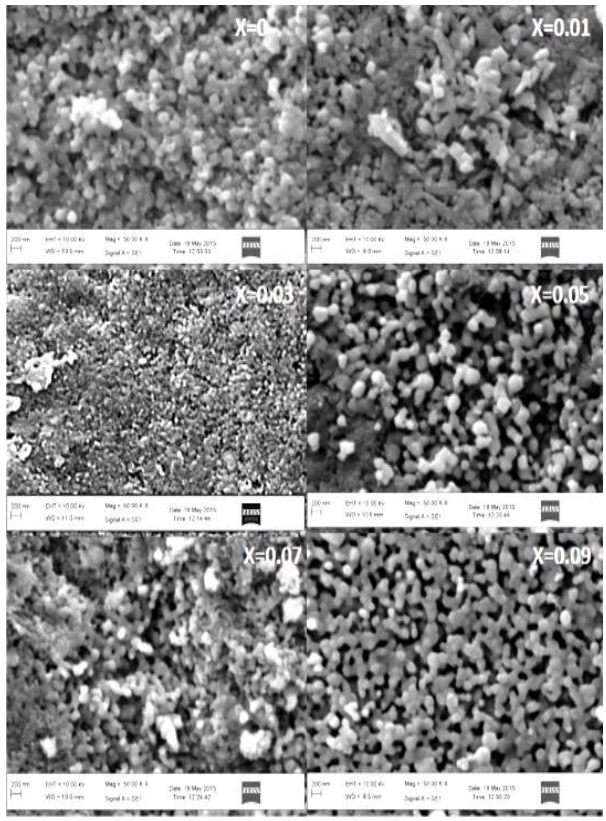

Fig. 3. SEM images of sintered $Mn_{0.6}Zn_{0.4}Fe_{2-x}Dy_xO_4$ ($0 \leq x \leq 0.09$) samples.

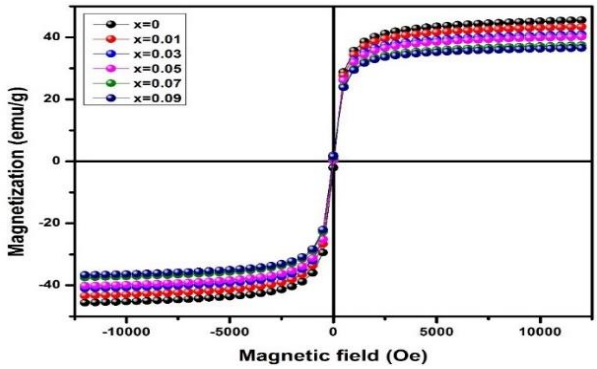

Fig. 4. Hysteresis loops for $Mn_{0.6}Zn_{0.4}Fe_{2-x}Dy_xO_4$ ($0 \leq x \leq 0.09$) samples

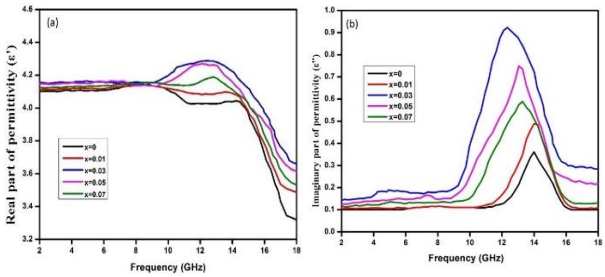

Fig. 5. (a) Real and (b) Imaginary parts of complex permittivity spectra of $Mn_{0.6}Zn_{0.4}Dy_xFe_{2-x}O_4$ (x=0.0, 0.01, 0.03, 0.05 and 0.07) samples.

The coercivity for the Dy doped Mn-Zn ferrites has been estimated from hysteresis loops and obtained values are presented in **Table 1**. It can be seen from the table that there is a significant increase in coercivity (H_c) with increase in dopant concentration. This trend is observed as magnetocrystalline anisotropy increases as Dy^{3+} replaces Fe^{3+} which also results in strong L-S coupling at octahedral site. Further such increase may be related to additional phase formation near grain boundaries impeding domain wall movement.

Complex permittivity and permeability are characteristic properties which represent dielectric and magnetic nature of materials **[27]**. The variations of complex permittivity ($\varepsilon=\varepsilon'-j\varepsilon''$) for $Mn_{0.6}Zn_{0.4}Dy_xFe_{2-x}O_4$ (x=0.0, 0.01, 0.03, 0.05 and 0.07) over frequency range of 2–18 GHz are shown in **Fig. 5**. It is found that the values of ε' for Dysprosium substituted Mn-Zn ferrite remain constant upto 10 GHz and shows a sudden fall where imaginary part have the resonance peak.. As a result of doping of Dysprosium in Mn-Zn ferrites, Fe^{3+} ion sites are replaced by Dy^{3+} ions, leading to higher concentration on ferrous ions (Fe^{2+}) than ferric ions (Fe^{3+}). Fe^{2+} ions are easily polarized results in enhanced interfacial polarization in turn increase in permittivity **[28, 29]**. The polarization of ferrites is explained through a hopping mechanism which is similar to conduction process. Therefore, the Dy^{3+} doping leads to increment of both dielectric polarization (ε') and dielectric loss (ε'') upto x=0.03. In addition, as the ionic radii of Dy^{3+} is bigger than that of Fe^{3+}, the lattice constant of $Mn_{0.6}Zn_{0.4}Fe_2O_4$ increases after doping. Thus, induced lattice strain causes dielectric losses. **[30]**. However, on further addition of Dy^{3+} leads to the additional phase formation at grain boundaries as confirmed by XRD patterns. . The additional phase may lead to decrease in availability of Dy^{3+} ions which further weakens the hopping mechanism as a result both the values decrease with Dy.

The real part of complex permeability **(Fig. 6)** values of the Mn-Zn ferrites doped with Dy^{3+} shows a higher value than that of pure Mn-Zn ferrite, and 0.03 mol% of Dy^{3+} doped Mn-Zn ferrite exhibits the highest real part of complex permeability. All the μ' values vary around 1.15. As can be observed from **Fig. 6**, μ″ has a peak at around 15 GHz, which is provoked by natural resonance **[31]**. It is also observed that the peak values of μ″ increases after the substitution of dysprosium. The values of μ″ increase with the increase in Dy^{3+} concentration and achieve highest when x=0.03and then it decreases for x >0.03 **(Fig. 6)**. This is due to increase in magneto -crystalline anisotropy of Dy^{3+}. In addition, when Dy is doped, the lattice distorts which leads to a higher value of μ″.

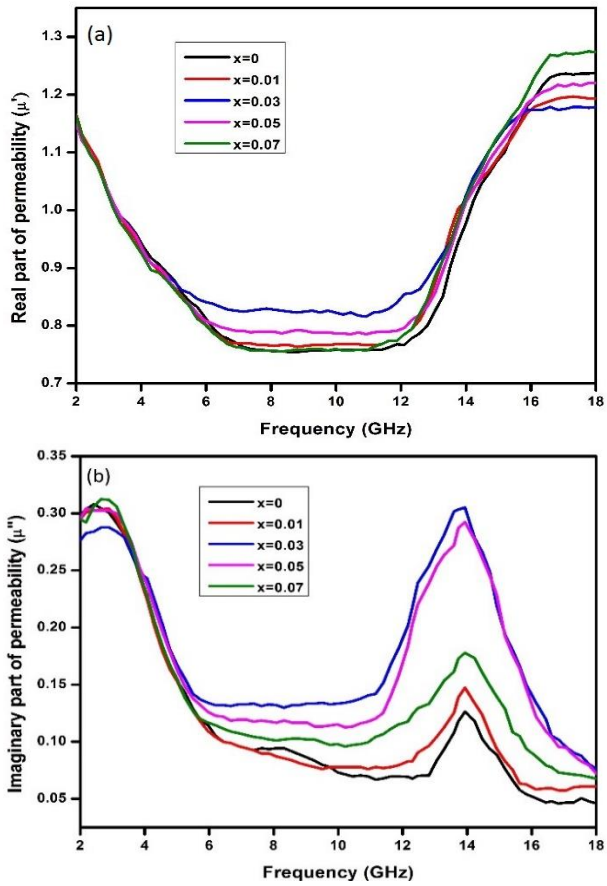

Fig. 6. (a) Real and (b) Imaginary parts of complex permeability spectra of $Mn_{0.6}Zn_{0.4}Dy_xFe_{2-x}O_4$ (x=0.0, 0.01, 0.03, 0.05 and 0.07) samples.

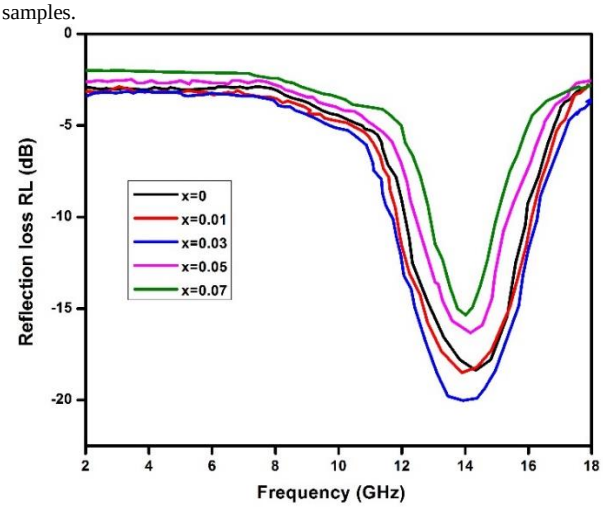

Fig. 7. Reflection loss curves (RL) for $Mn_{0.6}Zn_{0.4}Dy_xFe_{2-x}O_4$ (x=0.0, 0.01, 0.03, 0.05 and 0.07) samples.

The microwave absorbance of the samples can be predicted from a study of reflection loss (RL) in the materials. In general, the larger the negative value of RL, the greater the microwave absorption properties of

materials. Generally, the microwave absorption abilities result from the synergistic effect of the complex permittivity and permeability of the electromagnetic absorbing materials. Especially, the optimal wave absorption property may be induced when the electromagnetic match keeps a balance between magnetic loss and dielectric loss **[32]**.

The microwave absorbing properties of the materials can be defined by the reflection loss (RL) as shown in Eq. (2)-(3).

$$R.L.(dB) = 20\log_{10}\left|\frac{(Z_{in}-1)}{(Z_{in}+1)}\right| \quad (2)$$

$$Z_{in} = \left(\frac{\mu}{\varepsilon}\right)^{1/2} tanh\left[j\left(\frac{2\pi fd}{c}\right)\left(\frac{\mu}{\varepsilon}\right)^{1/2}\right] \quad (3)$$

where Z_{in} is the normalized input impedance related to the impedance in free space, $\varepsilon = \varepsilon'\text{-}j\varepsilon''$, $\mu = \mu'\text{-}j\mu''$ is the complex permeability and permittivity of the material, d is the thickness of the absorber, and c and f are the velocity of light and the frequency of microwave in free space, respectively. Z_{in}=1 is the impedance matching condition representing perfect absorbing properties. The impedance matching condition is determined by the combination of six parameters ε', ε", μ', μ", f and d. The calculated RL curves of the single-layer ferrite compound for Dy^{3+} doped MnZn ferrites at thickness of 2.3 mm are displayed in **Fig. 7**. Dy-substitution broadens the absorbing band. For x = 0.03 sample, RL reaches a maximum. The peak value of RL increases with the Dy^{3+} content $x < 0.05$, while it decreases a little when $x \geq 0.05$. The value of RL for x=0.03 is largest, which may be due to larger magnetic and dielectric losses. For x > 0.03 samples, additional phase formation lead to decrease in magnetic and dielectric losses. Hence decrease in RL is observed.

The $Mn_{0.6}Zn_{0.4}Fe_{1.97}Dy_{0.03}O_4$ ferrite showed good microwave absorption properties. The peak value of RL is about –20.5 dB with band width of 3.8 GHz. Thus microwave absorption properties of spinel ferrites can be effectively controlled by adjusting the rare earth doping concentration.

Conclusion

Manganese Zinc with rare earth Dy^{3+} doped mixed ferrite has been successfully prepared by microwave hydrothermal process**.** Increase in crystallite size upon substitution of Dy^{3+}ions in place of Fe^{3+} ion in ferrite lattice causes a significant change in the structural and electromagnetic properties. XRD disclose the cubic spinel phase of ferrite without other intermediate phase for x<0.05. FTIR analysis verifies the existence of tetrahedral and octahedral sites in the samples. We found appreciable increase in coercivity on increasing Dy^{3+} concentration due to distribution of cations and exchange interactions between the ions. The $Mn_{0.6}Zn_{0.4}Fe_{1.97}Dy_{0.03}O_4$ ferrite exhibited good microwave absorption properties of thickness of 2.3 mm in frequency range 2-18 GHz. This work focuses on relationship between synthesis technique and structure towards microwave absorption property. Thus rare earth doped spinel ferrites may be considered as a potential microwave absorption material.

References

1. Tong, C; Advanced materials and design for board level EMI shielding - Principle of board level shielding; BLS, **2012.**
2. Renlong Ji; Chuanbao Cao; Zhuo Chen; Huazhang Zhai; Ju Bai; *J. Mater. Chem. C*, **2014**, *2*, 5944.
3. Rabia Ahmad; Iftikhar Hussain Gul; Muhammad Zarrar; Humaira Anwar ; Muhammad Bilal Khan Niazi; Azim Khan; *J. Magn. Magn. Mater*, **2016,** *405*, 28.
4. Fengying Guo;Guijuan Ji; Jijing Xu; Haifeng Zou; Shucai Gan; Xuechun Xu; *J. Magn. Magn. Mater 324*, **2012**, 1209.
5. Yankui Cheng; Xiaohu Ren; *J. Supercond. Novel Magn.*, **2016,** *29*, 803.
6. Min Wang ; Guangbin Ji ; Baoshan Zhang ; Dongming Tang ;Yi Yang ;Youwei Du ; *J. Magn. Magn. Mater*. , *377*, **2015**, 52.
7. Chunming Yang ; Junjun Jiang; Xiaohua Liu; Chengjie Yin; Cuifen Deng; *J. Magn. Magn. Mater*, *404*, **2016,** 45.
8. Juhua Luo ; Yang Xu; Duoduo Gao; *Solid State Sci*. 37, **2014,** 40.
9. Juhua Luo; Yang Xu; Hongkai Mao; *J. Magn. Magn. Mater.*, 381, **2015,** 365.
10. Shital Patangrao Pawar; Dhruva Marathe, A.; Pattabhi, K.; Suryasarathi Bose; *J. Mater. Chem. A*, **2015**, 3, 656.
11. Bayat M.; Yang, H.; Ko, F.K.; Michelson, D.; Mei, A., J,Polym., JPOL, **2013**,16679.
12. Lu, X.; Liang. G.; Zhang. Y.; Wei Zhang; *Nanotechnology*, 18, **2007**, 015701.
13. Dong-Lin Zhao; Qiang Lv; Zeng-Min Shen; *J. Alloys Compd*., 480, **2009**, 63.
14. Xiaohu Ren, Guangliang Xu; *J. Magn. Magn. Mater.* 354, **2014,** 44.
15. Yan Wang, Xinming Wu, Wenzhi Zhang, Weixing Chen, *J. Magn. Magn.Mater*., 398 ,**2016**,90.
16. Wang, W. J; Jiao, Q. J.; Zang, C .G.;Zhu, X. D. *Adv. Mater. Res.* 30, **2011**, 415.
17. Wang, J., Zhang, H., Bai, S.X.; Chen, K.; Zhang, C.R.; *J. Magn. Magn. Mater.* 312, **2007**, 310
18. Waldron, R. D; *Phys. Rev. B: Solid State*, 99, **1955,** 263.
19. Shirsath, S. E. ; Jadhav, S. S. ; Toksha, B. G.; Patange, S. M.; Jadhav, K. M. ; *J. Appl. Phys*., **2011**, 110, 013914.
20. Pradhan, S. K; Bid, S; Gateshki, M.; Petkov, V.; *Mater. Chem. Phys*., 93, **2005**, 224.
21. Jiang, J.; Li, L.C.; Xu, F.; *J. Rare Earths*. 25, **2007**, 1, 79.
22. Rezlescu, N.; Rezlescu, E.; Popa, P.D.; Rezlescu. L.; *J. Alloys Compds.* 275, **1998**, 657.
23. Thankachan, Smitha; Binu, P.; Sheena, Xavier, Jacob; Mohammed, E., M., *J. Mag. Mag. Mat*. 348, **2013**, 140.
24. Kamala Bharathi K., Arout Chelvane J., Markandeyulu G., J. Magn. Magn. Mater, 321, **2009,** 3677.
25. Rezlescu, N.; Rezlescu E.; Pasnicu, C.; Craus, M. L.; *J. Phys.: Condens. Matter*, 6, **1994**, 29, 5707.
26 Zhao, Z.Y.; Wang, X.M.; Fan, C.; Tao, W.; Liu, X.G.; Ke, W.P.; Zhang, F.B.; Zhao, X.; Sun, X.F.; *Phys. Rev. B* ,**2011**, *83*, 014414
27. Cai, X. D.; Wang, J. J.; Liang, G. H.; Guo, J. S.; Hou, Y. S.; Gao, H. T.; Yu, L.; *J. Alloys Compds*. 636, **2015**, 348.
28. Xu, J. J.; Yang, C. M.; Zou, H. F.; Song, Y. H.; Gao, G. M.; An, B. C.; Gan, S. C.; *J. Magn. Magn. Mater*. 321, **2009**, 3231.
29. Deng, L. ; Ding, L.; Zhou, K.; Huang, S.; Hu, Z.; Yang, B.; *J. Magn. Magn. Mater*. 323, **2011** 1895.
30. Zhang, J.; Wang, L.; Hu, L. C.; Zeng, G.X.; Zhang H. Y.; *Materials Exploration and Application*. 21, **2006**, 33.
31. Sun, J.; Liu, J. H.; Li, S. M.; *J. Inorg. Mater*. 20, **2005,** 5, 1077.
32. Li, Y.Q.; Huang, Y.; Qi, S.H.; Niu, F.F.; Niu, L.; *J. Magn. Magn. Mater*. 323, **2011**, 2224.

